

https://dspace.org/

Imaging the African superplume - upper mantle, tomography and moment tensor

Brandt, Martin Barend Christopher

2012-10-01
http://hdl.handle.net/10539/11988

Downloaded from a DSpace repository. https://dspace.org/

New Regional Moment Tensors in South Africa

Martin B. C. Brandt and Ian Saunders
Council for Geoscience, South Africa

INTRODUCTION

Regional moment tensors (RMTs) provide important information for seismotectonic and hazard studies in regions with low to moderate seismicity, where infrequent earthquakes of $M_w \geq \sim 4.0–4.5$ occur that are too small for global moment-tensor techniques. Moment-tensor analysis involves fitting theoretical waveforms with observed broadband waveforms and inverting for the moment-tensor elements (*e.g.*, Aki and Richards 1980; Jost and Herrmann 1989). One powerful tool to calculate RMTs is the time domain surface wave waveform inversion code TDMT_INVC (Dreger and Helmberger 1993; Pasyanos *et al.* 1996; Dreger 2003). In recent years RMTs have been routinely calculated with this software in many parts of the world such as western Canada (Ristau *et al.* 2003, 2007), California (Dreger and Helmberger 1993; Romanowicz *et al.*1993; Pasyanos *et al.* 1996), Alaska (Ratchkovski and Hansen 2002), Japan (Kubo *et al.* 2002), Taiwan (Kao *et al.*1998), the European–Mediterranean region (Bernardi *et al.* 2004), and New Zealand (Ristau 2008).

Only a few moment tensors/focal mechanisms are available for South Africa. This is due to moderate tectonic and deep mine-related seismicity, as well as, until recently, a sparse distribution of broadband seismometers in the South African National Seismograph Network (SANSN) (Saunders *et al.* 2008). A unique opportunity presented itself when the dense, very broadband Incorporated Research Institutions in Seismology (IRIS) PASSCAL Kaapvaal craton array was deployed in South Africa (*e.g.*, Nguuri *et al.* 2001). From this array we identified three near regional M_w ~4.0 earthquakes with suitable waveform data to calculate RMTs with the TDMT_INVC software. Our goal is to determine the moment magnitude, earthquake mechanism, and focal depth in order to 1) make progress in resolving the difference between local and moment magnitudes routinely determined with the SANSN; and 2) expand our understanding of the regional seismotectonics and deep mine-related earthquakes.

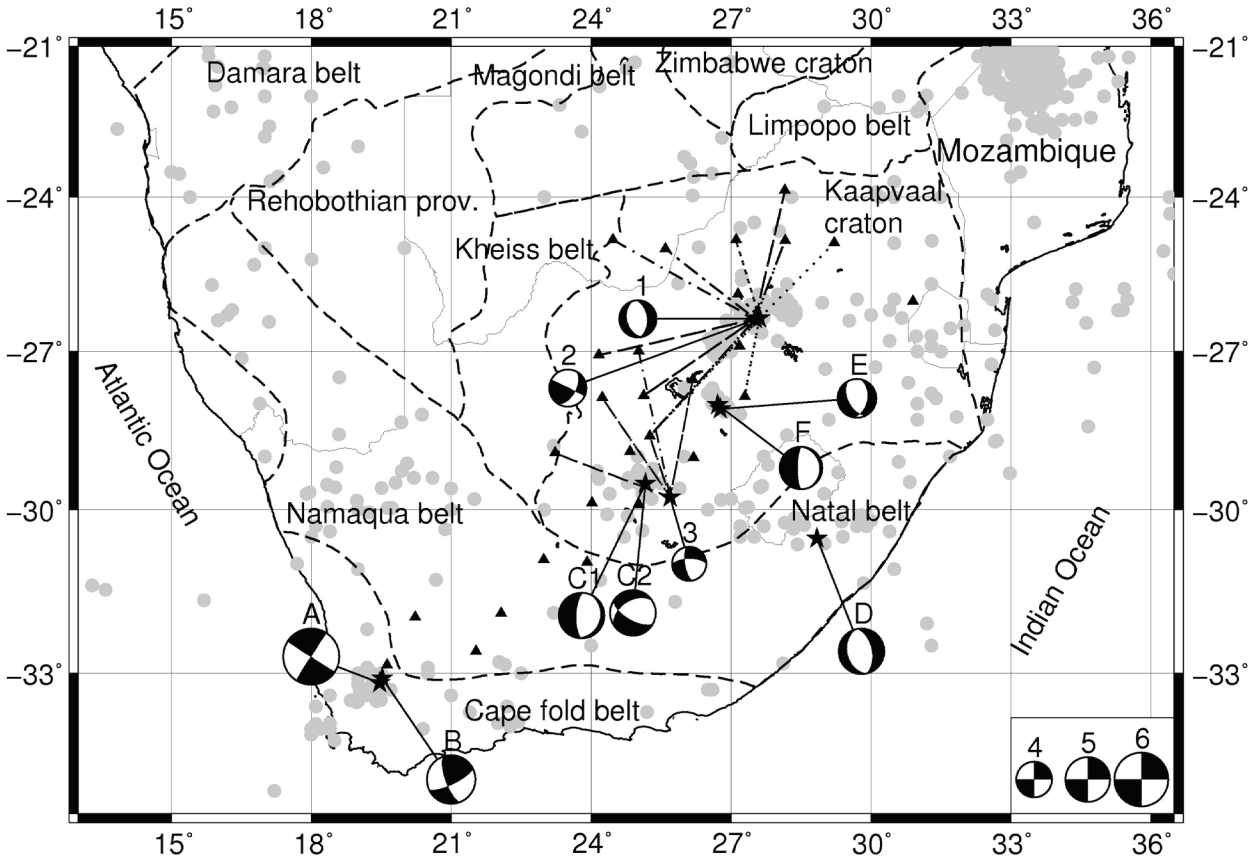
In this article we first review the regional seismotectonics and SANSN routine earthquake location procedures. Next, we select appropriate velocity and attenuation models as input for the TDMT_INVC software, invert three earthquake waveforms, and complete a sensitivity analysis to estimate the three solutions' reliability. Then we interpret the results with the seismotectonics. We also discuss our future plans to calculate moment magnitudes for the SANSN and derive an M_L–M_w relationship.

REGIONAL SEISMOTECTONICS AND ROUTINE EARTHQUAKE LOCATION

Earthquakes from the SANSN and historic databases with M_L larger and equal to 4 for the period 1620 to 2009 are shown in Figure 1. Previously published focal mechanisms/moment tensors are plotted as "beach balls" A (Fairhead and Girdler 1971; Green and McGarr 1972; Shudofsky 1985; Wagner and Langston 1988), B (Shudofsky 1985), C1 and C2 for event C (Fairhead and Stuart 1982; Shudofsky 1985), D (Dziewonski *et al.* 1987), E (Dziewonski *et al.* 1991), and F (Fan and Wallace 1995). We will derive new RMTs for earthquakes 1, 2, and 3 listed in Table 1. The faulting regime changes from normal in the northeast, near the east African rift with its higher seismicity, to strike-slip in the southwest. Tremors resulting from the deep mine operations in the gold fields (*e.g.*, 1, 2, E, and F) form the bulk of the seismic events recorded by the SANSN (Saunders *et al.* 2008). The largest principal stresses in Savuka mine, Far West Rand gold-mining area, are compressive, oriented near vertically, and are relaxed through a mix of volume closure and normal faulting for earthquakes with $0.5 < M_w < 2.6$ (Julià *et al.* 2009). The seismicity is shown with respect to the tectonic provinces of South Africa. The core of the Kalahari craton is comprised of the Archean Kaapvaal and Zimbabwe cratons connected by the Limpopo belt. Toward the south and west the surrounding mobile belts (Kheiss, Natal, Namaqua, Magondi, and Damara, as well as Rehobothian province) were fused to the cratons 2.6 Ga to 2.7 Ga ago, during which time the Kalahari craton and surrounding belts had become a stable assemblage. In the far south the Cape fold belt was extensively folded and thrusted during the breakup of the Gondwana super continent (*e.g.*, Johnson *et al.* 2006).

A number of crust and upper-mantle velocity models have been derived for South Africa from the IRIS Kaapvaal craton experiment data (*e.g.*, Larson *et al.* 2006; Li and Burke 2006; Nguuri *et al.* 2001; Saltzer 2002; Stankiewicz *et al.* 2002; Wright *et al.* 2002, 2003). Moho depth is especially well constrained (Nguuri *et al.* 2001; Niu and James 2002; Kwadiba *et al.* 2003). Most researchers found an undisturbed Archaean craton crust, typically thin (35 km to 40 km), unlayered, and with a strong velocity contrast across a sharp Moho discontinuity. From our experience, when locating earthquakes with the SANSN in the deep gold-mining areas with known hypocenters within 2 km (GT2 events), we conclude that our preferred 1-D model derived for the Kalahari craton (Table 2) works well, and we do not observe any significant azimuthal

doi: 10.1785/gssrl.82.1.69



▲ **Figure 1.** Location map of the seismic stations and earthquakes used in this study. Black stars represent the epicenters and triangles the stations. Moment-tensors/fault-plane solutions are indicated with "beach balls" with sizes proportional to magnitude. Previous solutions are marked with letters A to F and new moment tensors by numbers 1 to 3. Dotted and dash-dot lines show where waves propagate between earthquakes 1 to 3 and the stations used for the moment tensor inversions; other stations were used for the fault plane solution. Major tectonic provinces are separated with thick dashed lines and are labeled. Earthquakes from 1620 to 2009 with local magnitude larger than and equal to 4 are plotted with gray dots. For details of the solutions, see text.

TABLE 1
Event Parameters of the Earthquakes Used in This Study and Their Calculated Moment Magnitudes

	Date	Lat.	Lon.	Depth (km)	Ms ISC	ML PRE	Mw	Remarks
1	97-09-25	-26.37	27.52	2	3.7	4.5	4.1	Mine-related earthquake.
2	98-12-05	-26.36	27.61	2	3.9	4.3	4.1	Mine-related earthquake.
3	99-02-04	-29.76	25.70	5	N/D	4.5	3.8	Compare with event C1 & 2.

ISC = International Seismological Centre
PRE = Council for Geoscience, Pretoria

dependence. We only observe time delays for earthquakes in the Cape fold belt or Mozambique. Table 2 consists of *P*- and *S*-wave velocities from Wright *et al.* (2002; 2003) (modified for Moho depth) and density from the global IASP91 model (Kennett *et al.* 1995).

The *P*- and *S*-wave attenuation in Table 2, Q_p and Q_s respectively, are adapted for the Kalahari craton from Dziewonski and Anderson (1981). There are no published regional attenuation studies available for South Africa. Our best guess is that the stable, Archean Kalahari craton could be similar to the Canadian shield. Values for Q_s in stable continental regions vary (Padhy 2005) from, for example, 273 (Mexico), 380 (eastern and western Canada), and 460 (Indian shield) to 680 (eastern and northern America), and for active continental areas from 50 (Himalaya), 83 (Kanto, Japan), and 180 (southern California) to 238 (Great Basin).

Tectonic events in southern Africa are assumed to be shallow, *i.e.*, in the upper crust. For routine location with the

TABLE 2
South African Velocity Model

Depth (km)	Layer thickness (km)	*Vp* (km/s)	*Vs* (km/s)	Density (g/cm^3)	*Qp*	*Qs*
0.0	5.0	5.761	3.462	2.7	700	350
5.0	5.0	6.018	3.553	2.7	700	350
10.0	5.0	6.210	3.659	2.7	700	350
15.0	5.0	6.419	3.752	2.7	700	350
20.0	0.1	6.591	3.806	2.7	700	350
20.1	6.9	6.800	3.926	2.9	700	350
27.0	11.0	6.950	3.954	2.9	700	350
38.0	0.1	7.100	3.982	2.9	700	350
38.1	6.9	8.035	4.639	3.2	700	350
45.0	5.0	8.049	4.647	3.2	700	350
50.0	10.0	8.059	4.653	3.2	700	350
60.0	10.0	8.067	4.658	3.2	700	350
70.0	10.0	8.080	4.665	3.2	700	350
80.0	10.0	8.094	4.673	3.2	700	350
90.0	Inf.	8.112	4.683	3.3	700	350

SANSN we fix the focal depths at 5 or 10 km for tectonic earthquakes and 2 km for mine-related tremors (Saunders *et al.* 2008). However, we approached the International Seismological Centre (ISC) to relocate earthquakes A and C with both local and global phases to verify this assumption. The ISC fixed the depth for the 1969 earthquake to 10 km because of insufficient local phases, but a reliable depth of between 7 km and 11 km could be determined for the 1976 event (Dmitry Storchak, personal communication, 2008).

We will investigate the effect of focal depth, attenuation, and epicenter uncertainty on our RMTs reliability with a sensitivity analysis.

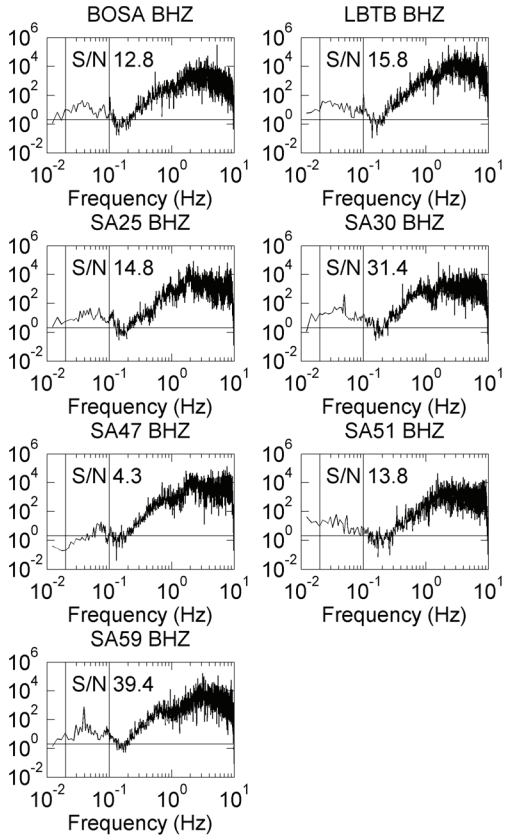
DATA, EVENT SELECTION, AND PROCESSING

The Kaapvaal craton seismic experiment consisted of 55 broadband REFTEK/STS2 instruments deployed at 81 sites between April 1997 and July 1999. The seismometers were arranged along a roughly NE–SW axis in southern Africa and were installed in South Africa, Botswana, and Zimbabwe at ~1 degree intervals, which is significantly denser than for the SANSN. The continuously recorded data of the portable experiment were supplemented by data from three stations of the International Monitoring System in the region of the array (*e.g.*, Nguuri *et al.* 2001). We used seismic waveform data produced by three earthquakes (two mine-related and one tectonic) in South Africa (Figure 1; Table 1).

In areas of the world where regional moment-tensor solutions are routinely calculated for magnitudes around 4, the observed waveforms are typically bandpass-filtered between 0.1 and 0.02 Hz (*e.g.*, Ristau *et al.* 2007; Braunmiller and Nabelek 2002; Ratchkovski and Hansen 2002; Kao *et al.* 1998; Dreger and Helmberger 1993). In this frequency range the seismograms are dominated by guided and surface waves, which can be adequately modeled using 1-D velocity structures. We searched for earthquakes recorded by five or more stations between 30 km and 400 km distance with average signal-to-noise ratio above two in the frequency range between 0.02 and 0.1 Hz. Average signal-to-noise ratios of the vertical component for earthquakes 1 to 3 are shown as Figures 2, 3 and 4. It should be noted that the earthquake on 22 April 1999 in the Free State gold-mining area with $M_s = 4.7$ (as reported by the ISC) saturated all the Kaapvaal craton array seismographs within 400 km distance, which meant that the event could not be used in our study.

We opted to use the manual code as it is expected that only a few RMTs would be calculated in South Africa. The code is designed to obtain reliable solutions using a minimal number of stations: typically only two or three three-component broadband stations are required to obtain an acceptable solution (Dreger and Helmberger 1993). Preparation of the observed waveforms is a relatively simple process consisting of the following: 1) removing the instrument response, 2) rotation of the horizontal components to radial and transverse components, 3) integration to convert to displacement, 4) bandpass filtering between 0.02 Hz and 0.1 Hz, and 5) re-sampling the data to 1 sample per second to match the Green's functions. The Green's functions are also filtered with the same bandpass filter as the observed data.

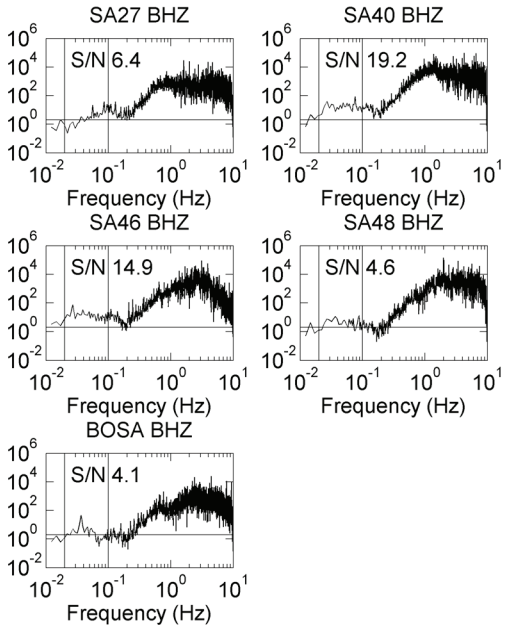
We used the same 1-D velocity structure for calculating the Green's functions to model the observed waveforms at regional distances as the one used for routine earthquake analysis by the SANSN (see previous section and Table 2). If the Green's functions are not representative of the true Earth structure at the



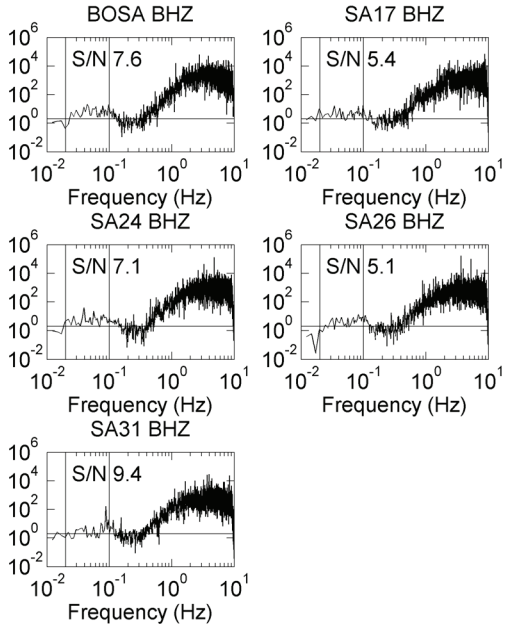
▲ **Figure 2.** Signal-to-noise ratio for the vertical component of the seven stations used to calculate regional moment-tensor solution one of Table 1 for the Far West Rand gold- mining area in Figure 5. The horizontal line indicates a ratio of two and vertical lines indicate frequencies between 0.02 and 0.1 Hz used in the processing. Average signal-to-noise ratio is listed as S/N.

frequencies being used the resulting moment-tensor solutions will not be reliable. The small source-receiver distances (<400 km) help to reduce possible errors introduced by differences between the velocity model and the true Earth structure such as scattering effects and phase shifts. We also constrain the isotropic component for the moment tensor elements to zero for increased numerical stability. Fortunately the Kalahari craton has a simple velocity structure, and most of the seismographs used are confined to the Kaapvaal craton. We determined focal depths iteratively by finding the depth that yields the largest variance reduction between the observed and synthetic waveforms and/or the largest major-versus-minor double-couple for the moment-tensor solutions.

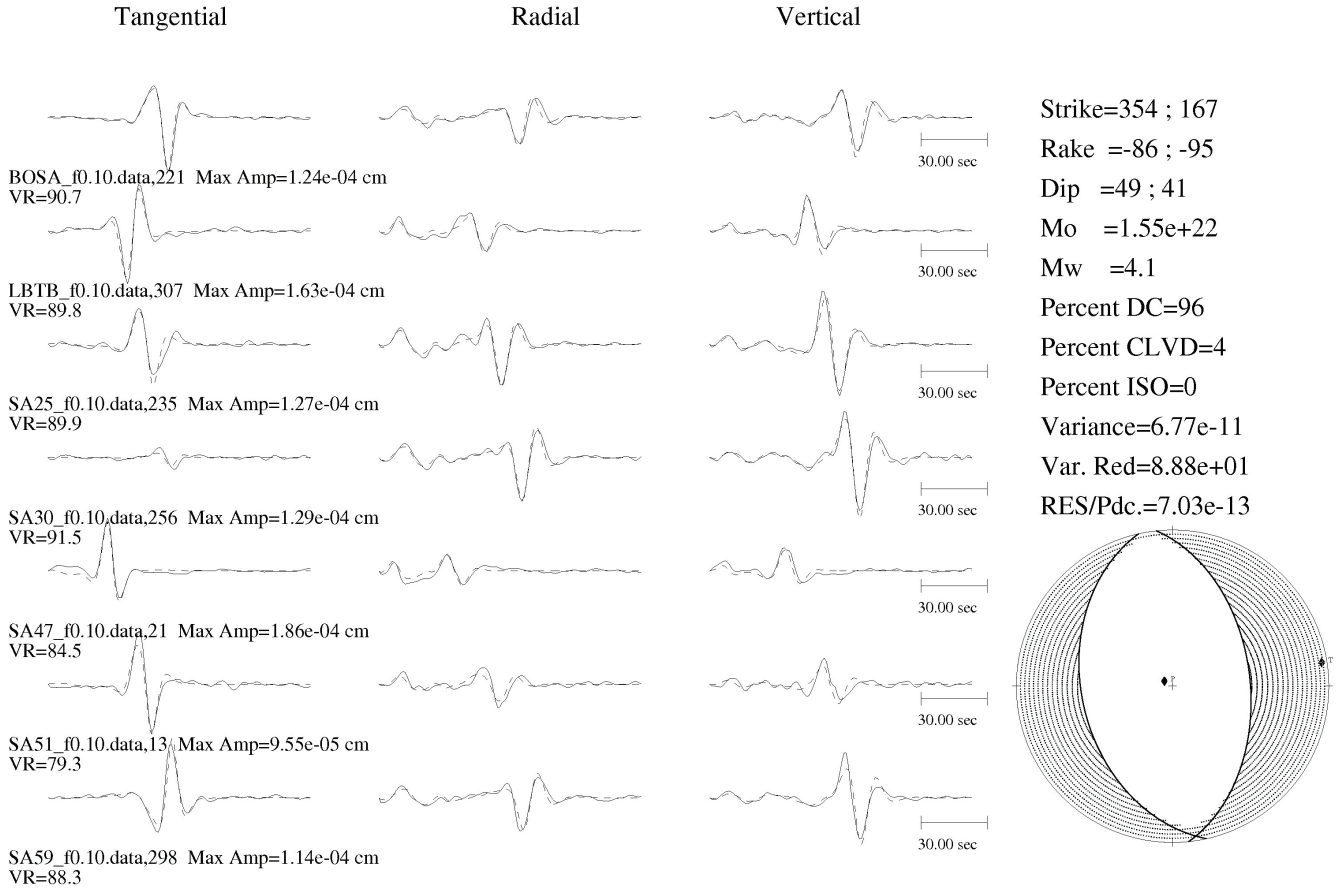
Unfortunately it is not possible to calibrate the regional moment-tensor solutions against reference events from the global centroid moment tensor (GCMT) catalog. We could only compare our solutions with previously published focal mechanisms/moment tensors A to F and to what is known about the general seismotectonics/deep mining-related seismicity of the region (Figure 1; Julià *et al.* 2009). We will determine a fault plane solution for event no. 3.



▲ **Figure 3.** Signal-to-noise ratio for the vertical component of the five stations used to calculate regional moment-tensor solution two of Table 1 for the Far West Rand gold- mining area in Figure 8. The horizontal line indicates a ratio of two and vertical lines indicate frequencies between 0.02 and 0.1 Hz used in the processing. Average signal-to-noise ratio is listed as S/N.



▲ **Figure 4.** Signal-to-noise ratio for the vertical component of the five stations used to calculate regional moment-tensor solution three of Table 1 for the Fauresmith area in Figure 11. The horizontal line indicates a ratio of two and vertical lines indicate frequencies between 0.02 and 0.1 Hz used in the processing. Average signal-to-noise ratio is listed as *S/N*.



▲ **Figure 5.** Regional moment-tensor solution with $M_w = 4.1$ for mine-related earthquake one in Table 1 that occurred in the Far West Rand deep gold-mining area. Solid lines show the waveform data, and the synthetic seismograms are indicated by dashed lines. The solution, namely the strike, rake, and dip of the fault and auxiliary planes; seismic moment in dyne·cm; and moment magnitude are listed on the right. The moment-tensor decomposition in terms of percent major double-couple (DC) and percent minor double-couple, represented by the compensated linear vector dipoles (CLVD), as well as percent isotropic component (ISO) (set to zero), are listed underneath. The reliability of the solution is quantified by the variance, variance reduction, and variance divided by the percent double-couple. For details of this solution, see text.

MOMENT-TENSOR SOLUTIONS AND SENSITIVITY ANALYSIS

1997-09-25 Far West Rand Gold Mines

Seven stations with source-receiver distances of <400 km were used in this solution (Figure 1). A comparison between the synthetic and observed waveform in Figure 5 shows that the fit varies from good (variance reduction VR = 79.3%) to excellent (91.5%). We derived a double-couple normal-faulting focal mechanism with the *P*-axis in the vertical direction and the *T*-axis oriented east-northeast. A depth of 2 km yields a large variance reduction between the observed and synthetic waveforms and the highest double-couple percentage (Figure 6). No global or regional moment-tensor solutions had been derived before this study in the Far West Rand gold-mining area. However, a sensitivity study indicates that changes to the solution and misfit parameters are insignificant for reasonable changes in attenuation ($Q_p = 600$ and $Q_p = 800$) and epicenter uncertainty (10 km north and 10 km east) (Figure 7). Only moment magnitude is sensitive to the focal depth ($M_w = 4.0$ to $M_w = 4.2$), but this could be due to this mine-related earthquake's very shallow hypocenter. The derived focal mechanism and stress directions are consistent with previous solutions for earthquakes D, E, and F. All these solutions were produced in an east-west principal extensional-stress system. Our solution compares well with the normal faulting regime for Savuka mine found by Julià *et al.* (2009) but without the volume closure. There is a discrepancy between $M_L = 4.5$ and the calculated $M_w = 4.1$ for this event. The next two solutions will show that differences between M_L and M_w are a recurring issue for South Africa, and will be discussed in more detail below.

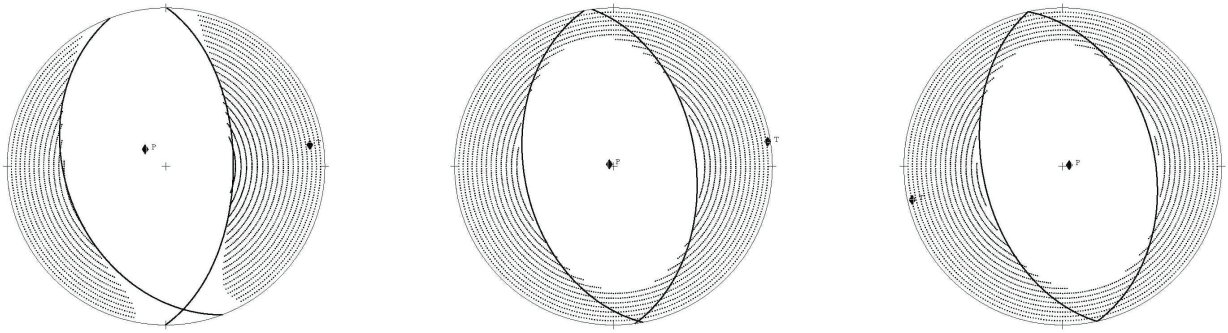
1998-12-05 Far West Rand Gold Mines

Five stations with source-receiver distances of <400 km were used in this solution (Figure 1; Figure 8). We derived an oblique strike-slip focal mechanism with the *P*-axis in the north-northwest direction and the *T*-axis toward the west-southwest. A depth of 1 km yields the largest variance reduction between the observed and synthetic waveforms and the highest double-couple percentage (Figure 9). As was the case with the

Strike=0 ; 159
Rake =-78 ; -107
Dip =55 ; 37
Mo =1.24e+22
Mw =4.0
Percent DC=78
Percent CLVD=22
Percent ISO=0
Variance=9.52e-11
Var. Red=8.40e+01
RES/Pdc.=1.23e-12

Strike=352 ; 169
Rake =-88 ; -92
Dip =47 ; 43
Mo =2.03e+22
Mw =4.2
Percent DC=72
Percent CLVD=28
Percent ISO=0
Variance=6.17e-11
Var. Red=9.00e+01
RES/Pdc.=8.58e-13

Strike=168 ; 347
Rake =-90 ; -90
Dip =48 ; 42
Mo =2.07e+22
Mw =4.2
Percent DC=68
Percent CLVD=32
Percent ISO=0
Variance=1.84e-10
Var. Red=6.72e+01
RES/Pdc.=2.71e-12



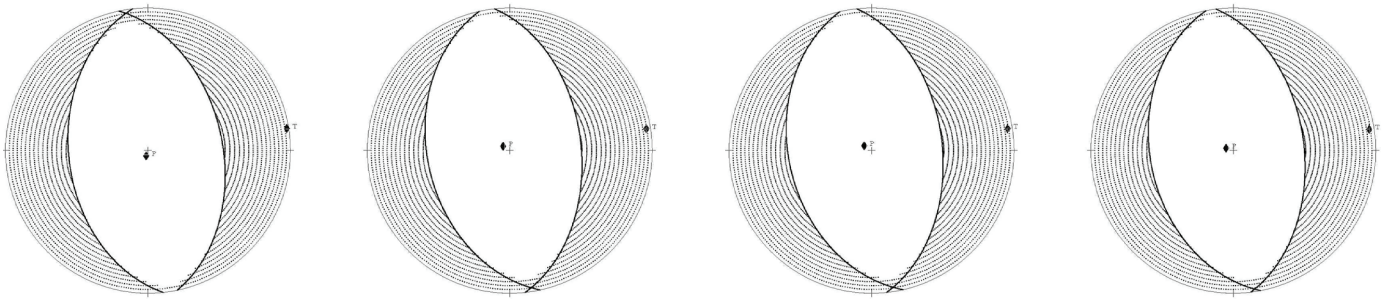
▲ **Figure 6.** Regional moment-tensor solution with M_w = 4.1 for mine-related earthquake one in Table 1 with depths of 1 km, 3 km, and 4 km (from left to right). All other input parameters/velocity model are the same as for Figure 5.

Strike=348 ; 174
Rake =-94 ; -86
Dip =47 ; 44
Mo =1.56e+22
Mw =4.1
Percent DC=96
Percent CLVD=4
Percent ISO=0
Variance=6.60e-11
Var. Red=8.90e+01
RES/Pdc.=6.85e-13

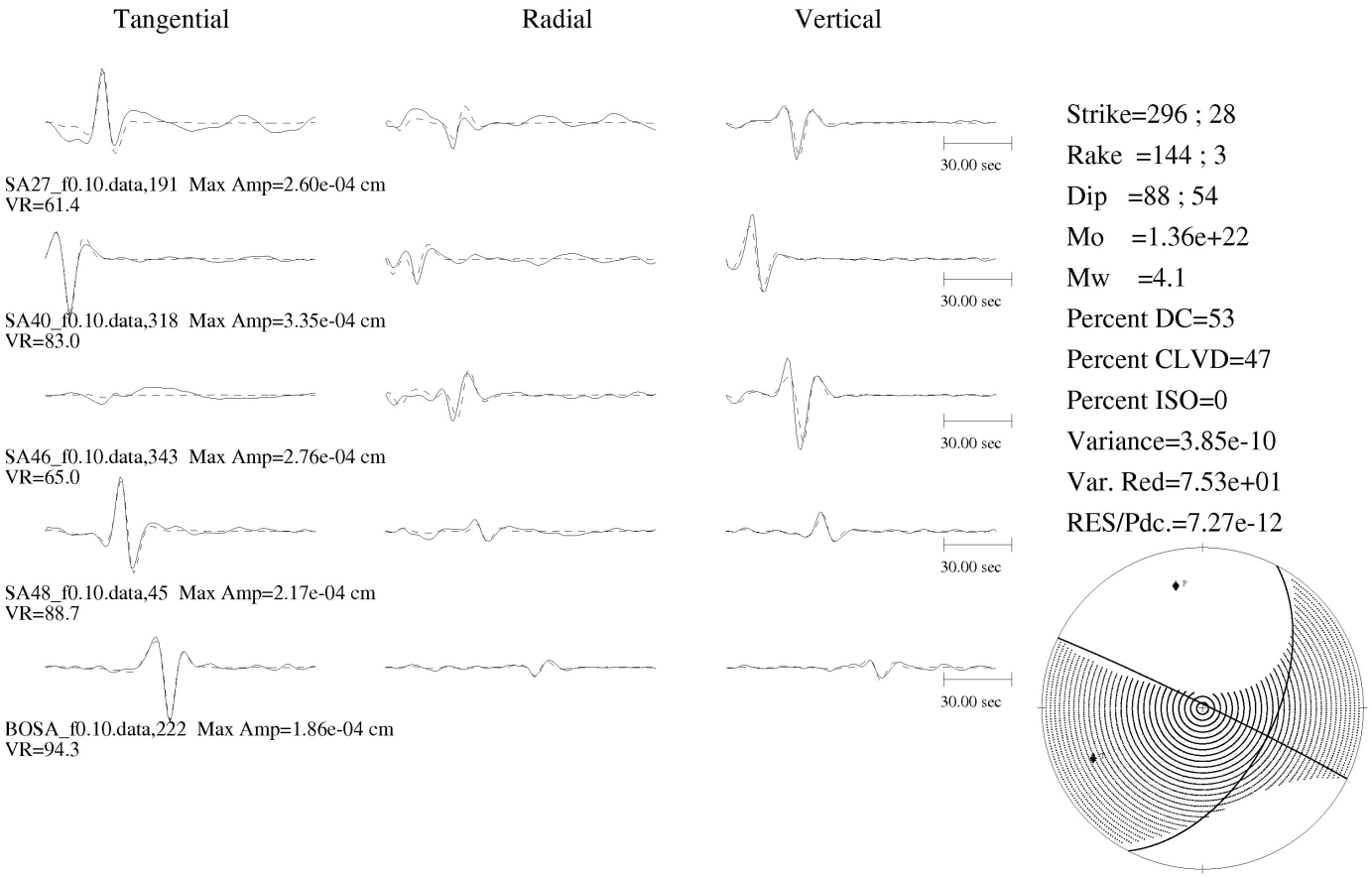
Strike=354 ; 168
Rake =-86 ; -95
Dip =48 ; 42
Mo =1.54e+22
Mw =4.1
Percent DC=96
Percent CLVD=4
Percent ISO=0
Variance=6.88e-11
Var. Red=8.86e+01
RES/Pdc.=7.14e-13

Strike=354 ; 167
Rake =-85 ; -95
Dip =49 ; 41
Mo =1.55e+22
Mw =4.1
Percent DC=97
Percent CLVD=3
Percent ISO=0
Variance=6.83e-11
Var. Red=8.87e+01
RES/Pdc.=7.08e-13

Strike=353 ; 169
Rake =-87 ; -93
Dip =49 ; 41
Mo =1.54e+22
Mw =4.1
Percent DC=96
Percent CLVD=4
Percent ISO=0
Variance=7.89e-11
Var. Red=8.73e+01
RES/Pdc.=8.18e-13



▲ **Figure 7.** Regional moment-tensor solution with M_w = 4.1 for mine-related earthquake one in Table 1 with attenuations Q_p = 600; Q_p = 800, epicenter 10 km to the north, and epicenter 10 km to the east (from left to right). All other input parameters/velocity model are the same as for Figure 5.



▲ **Figure 8.** Regional moment-tensor solution with $M_w = 4.1$ for mine-related earthquake two in Table 1 that occurred in the Far West Rand deep gold-mining area. Solid lines show the waveform data, and the synthetic seismograms are indicated by dashed lines. The solution, namely the strike, rake, and dip of the fault and auxiliary planes; seismic moment in dyne·cm; and moment magnitude are listed on the right. The moment-tensor decomposition in terms of percent major double-couple (DC) and percent minor double-couple, represented by the compensated linear vector dipoles (CLVD), as well as percent isotropic component (ISO) (set to zero), are listed underneath. The reliability of the solution is quantified by the variance, variance reduction, and variance divided by the percent double-couple. For details of this solution, see text.

1997 solution a sensitivity study indicates that the solution is insensitive to reasonable changes in attenuation ($Q_p = 600$ and $Q_p = 800$) and epicenter uncertainty (10 km north and 10 km east) (Figure 10). Moment magnitude changes slightly from $M_w = 4.0$ to $M_w = 4.1$ with focal depth. The derived focal mechanism differs from previous solutions D, E, and F as well as the normal faulting regime for Savuka mine found by Julià *et al.* (2009). Note the solution's decomposition into 53% major versus 47% minor double couple. This could be due to low overburden pressure for this very shallow event resulting in horizontal *P*- and *T*-axes, or the source could have a significant percentage volume closure as was found by Julià *et al.* (2009) for smaller magnitudes. We completed a full moment-tensor inversion, where the isotropic component is allowed to vary, but this solution is unstable. Again, there is a discrepancy between the calculated $M_L = 4.3$ and $M_w = 4.1$ for this event.

1999-02-04 Fauresmith Area in the Koffiefontein Cluster

Five stations with source-receiver distances of <400 km were used in this solution (Figure 1; Figure 11). We derived a double-couple oblique normal fault focal mechanism with the *P*-axis dipping toward the southeast and the *T*-axis in the southwest direction. A depth of 11 km yields the largest variance reduction between the observed and synthetic waveforms and the highest double-couple percentage (Figure 12). As before, a sensitivity study indicates that the solution is insensitive to reasonable changes in attenuation ($Q_p = 600$ and $Q_p = 800$) and epicenter uncertainty (10 km north and 10 km east) (Figure 13). Moment magnitude remains constant at $M_w = 3.8$ for this deeper event. The derived focal mechanism and stress orientation differ from previous solutions C1 and C2 derived for earthquake C (Figure 1; Fairhead and Stuart 1982; Shudofsky 1985). Again, there is a discrepancy between the magnitudes ($M_L = 4.5$ as opposed to $M_w = 3.8$) for this event.

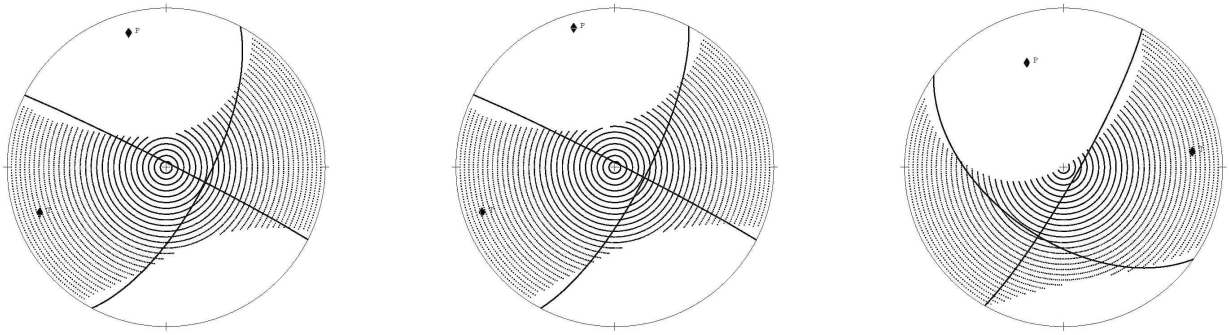
Comparison with First-motion Fault-plane Solutions and Location Depth

We calculated first-motion fault-plane solutions for all three earthquakes using the program by Snoke (2003). This program performs a grid search to determine how many polarities satisfy

Strike=297 ; 28
Rake =159 ; 2
Dip =88 ; 69
Mo =1.26e+22
Mw =4.0
Percent DC=43
Percent CLVD=57
Percent ISO=0
Variance=3.98e-10
Var. Red=7.47e+01
RES/Pdc.=9.26e-12

Strike=297 ; 28
Rake =164 ; 2
Dip =88 ; 74
Mo =1.28e+22
Mw =4.0
Percent DC=34
Percent CLVD=66
Percent ISO=0
Variance=4.41e-10
Var. Red=7.22e+01
RES/Pdc.=1.30e-11

Strike=30 ; 125
Rake =-37 ; -171
Dip =83 ; 53
Mo =1.54e+22
Mw =4.1
Percent DC=39
Percent CLVD=61
Percent ISO=0
Variance=4.78e-10
Var. Red=6.96e+01
RES/Pdc.=1.22e-11



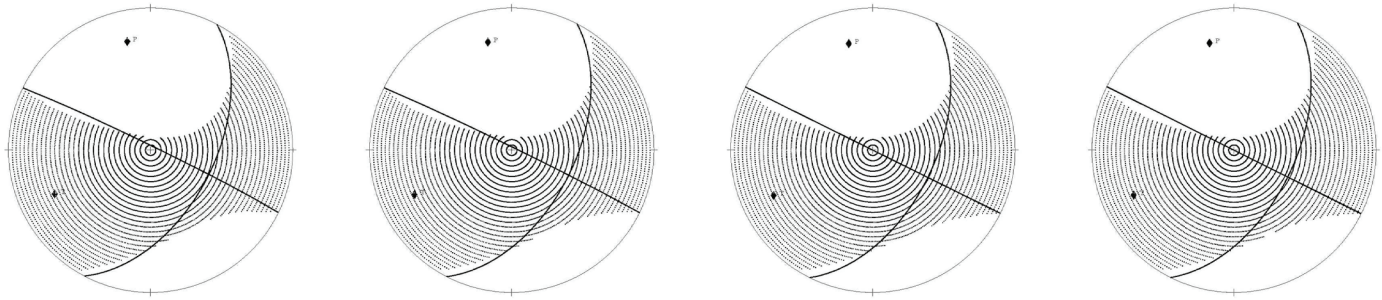
▲ **Figure 9.** Regional moment-tensor solution with M_w = 4.1 for mine-related earthquake two in Table 1 with depths of 2 km, 3 km, and 4 km (from left to right). All other input parameters/velocity model are the same as for Figure 8.

Strike=296 ; 28
Rake =144 ; 3
Dip =88 ; 54
Mo =1.37e+22
Mw =4.1
Percent DC=56
Percent CLVD=44
Percent ISO=0
Variance=3.88e-10
Var. Red=7.51e+01
RES/Pdc.=6.93e-12

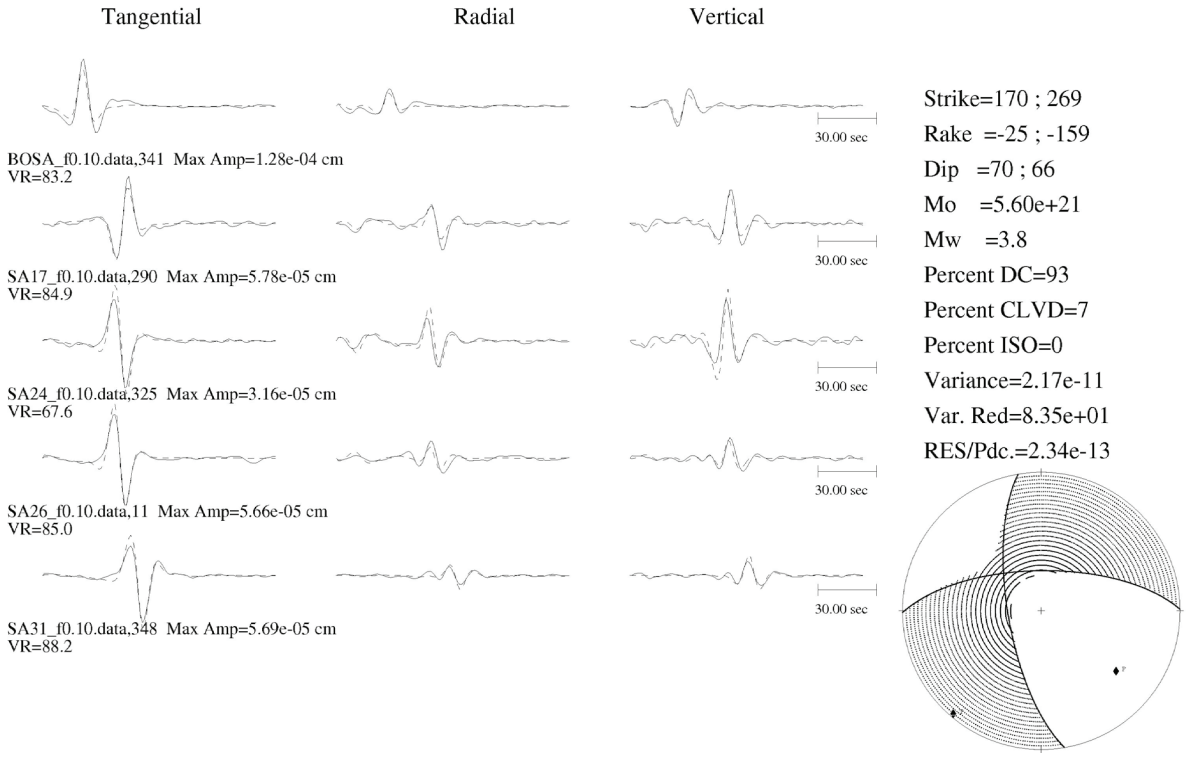
Strike=296 ; 27
Rake =144 ; 2
Dip =88 ; 54
Mo =1.36e+22
Mw =4.1
Percent DC=51
Percent CLVD=49
Percent ISO=0
Variance=3.83e-10
Var. Red=7.55e+01
RES/Pdc.=7.56e-12

Strike=296 ; 26
Rake =144 ; 0
Dip =90 ; 54
Mo =1.36e+22
Mw =4.1
Percent DC=43
Percent CLVD=57
Percent ISO=0
Variance=3.94e-10
Var. Red=7.50e+01
RES/Pdc.=9.09e-12

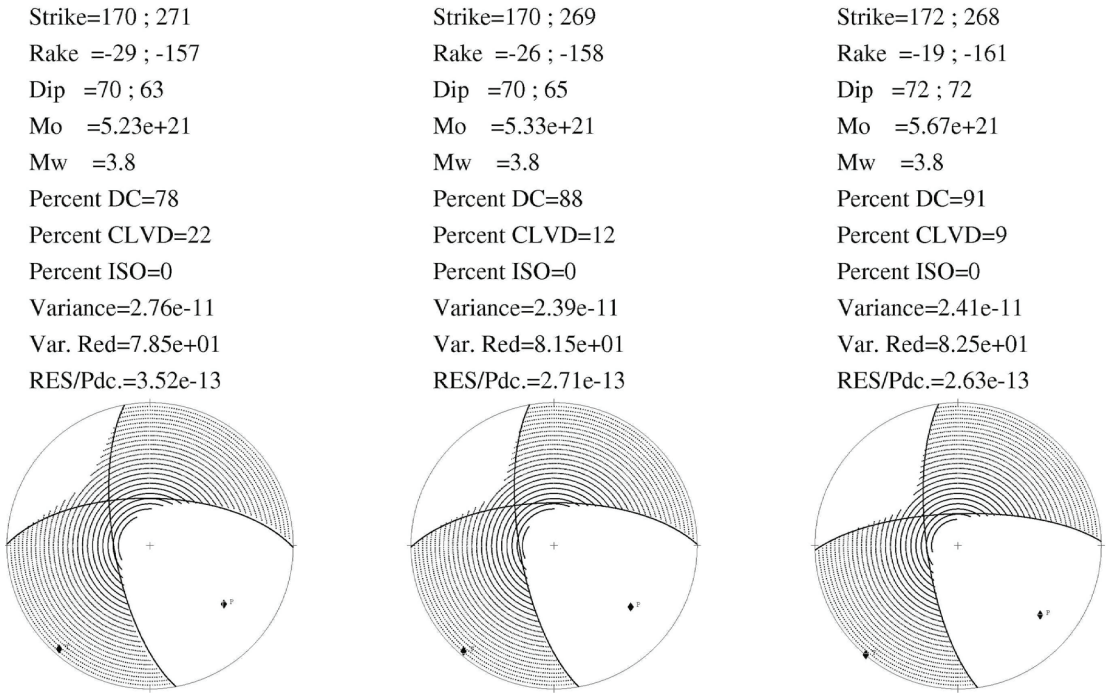
Strike=117 ; 27
Rake =-145 ; -0
Dip =90 ; 55
Mo =1.35e+22
Mw =4.1
Percent DC=44
Percent CLVD=56
Percent ISO=0
Variance=3.91e-10
Var. Red=7.51e+01
RES/Pdc.=8.83e-12



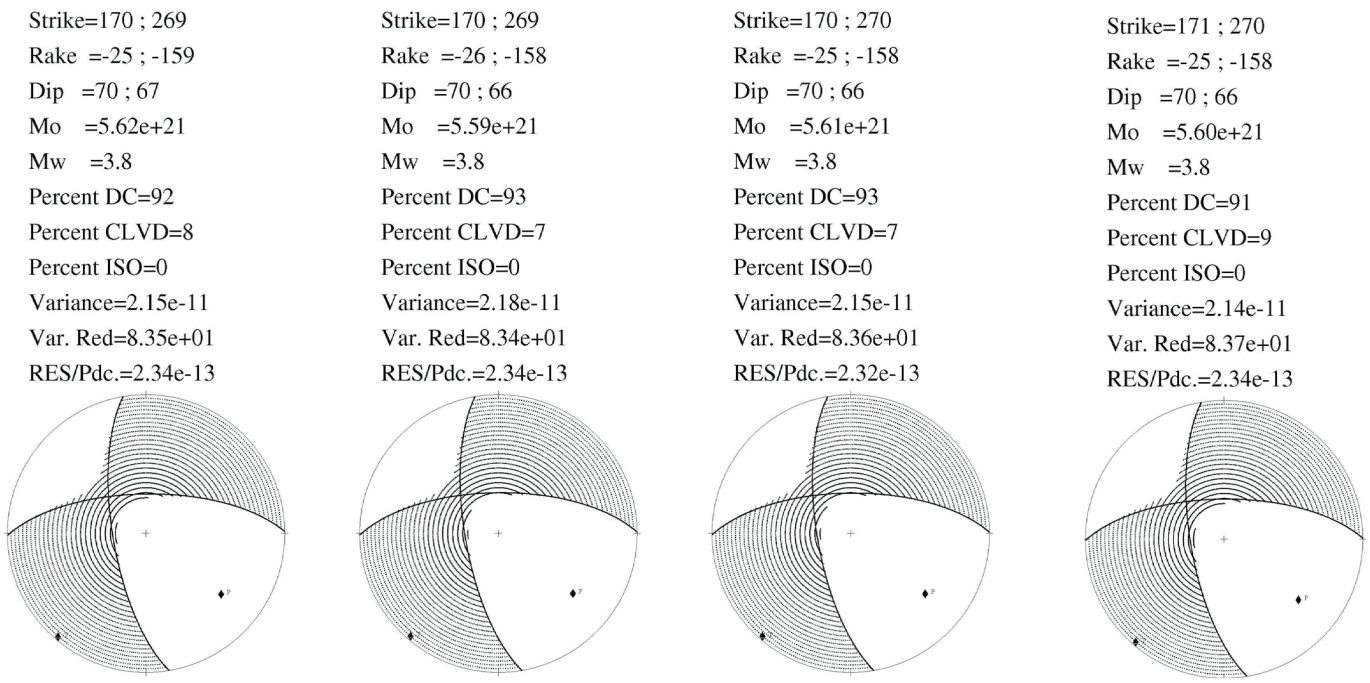
▲ **Figure 10.** Regional moment-tensor solution with M_w = 4.1 for mine-related earthquake two in Table 1 with attenuations Q_p = 600, Q_p = 800, epicenter 10 km to the north, and epicenter 10 km to the east (from left to right). All other input parameters/velocity model are the same as for Figure 8.



▲ **Figure 11.** Regional moment-tensor solution with M_w = 3.8 for tectonic earthquake three in Table 1 that occurred in the Fauresmith area. Solid lines show the waveform data, and the synthetic seismograms are indicated by dashed lines. The solution, namely the strike, rake, and dip of the fault and auxiliary planes; seismic moment in dyne·cm; and moment magnitude are listed on the right. The moment-tensor decomposition in terms of percent major double-couple (DC) and percent minor double-couple, represented by the compensated linear vector dipoles (CLVD), as well as percent isotropic component (ISO) (set to zero), are listed underneath. The reliability of the solution is quantified by the variance, variance reduction, and variance divided by the percent double-couple. For details of this solution, see text.



▲ **Figure 12.** Regional moment-tensor solution with M_w = 3.8 for tectonic earthquake three in Table 1 with depths of 7 km, 9 km, and 13 km (from left to right). All other input parameters/velocity model are the same as for Figure 11.



▲ **Figure 13.** Regional moment-tensor solution with $M_w = 3.8$ for tectonic earthquake three in Table 1 with attenuations $Q_p = 600$, $Q_p = 800$, epicenter 10 km to the north, and epicenter 10 km to the east (from left to right). All other input parameters/velocity model are the same as for Figure 11.

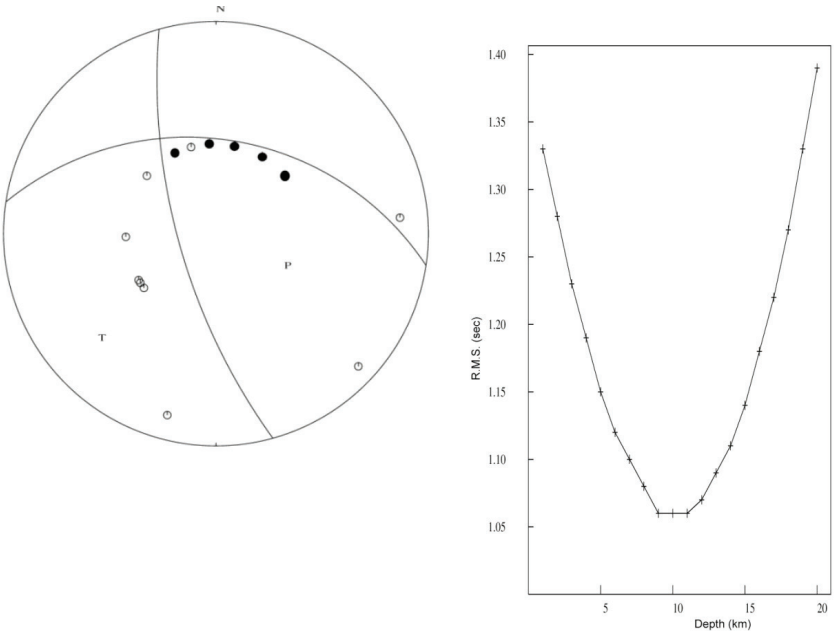
each possible solution. First-motion solutions require a large number of stations with good azimuthal coverage and varying distances. This makes the data from the Kaapvaal craton array well suited for such a study (Figure 1). Earthquakes 1 and 2 have only a few impulsive onsets, hence no fault planes could be determined for comparison with their respective moment-tensor solutions. This is not uncommon since we rarely observed clear impulsive onsets for mine-related earthquakes when analyzing data from the SANSN. We suspect that the emergent onsets could be attributable to brittle failure in the uppermost crust. We were able to calculate a fault-plane solution for the tectonic earthquake (referred to in this paper as event no. 3) namely: strike = 164, rake = -53, and dip = 70 (Figure 14). This is similar to the oblique normal fault in Figure 11. Note that previous solutions C1 (first-motion polarities) and C2 (body-wave modeling) contradicted each other, which is not the case here. We obtained a similar focal depth of between 9 km and 11 km with P_n, P_g, S_n, and S_g phases by determining the root-mean-square time residual as a function of depth with the location program HYPOCENTER (Lienert and Havskov 1995) (Figure 14) for the velocity model in Table 2.

DISCUSSION

The discrepancy between local and moment magnitude is not unexpected. M_L calculation in South Africa is based on the relation of Hutton and Boore (1987) for southern California, which is essentially the same as Richter's (1935) original definition for magnitude. The tectonic setting of South Africa differs significantly from southern California, which affects the attenuation of wave energy with distance. We routinely observe overestimation of M_L with increasing epicentral distance when locating earthquakes with the SANSN: this overestimation becomes severe with ~1 to 1.5 units for stations at far regional distances. M_L standard deviation typically ranges between 0.2 and 0.4 units, but we do not expect a linear M_L–M_w relationship. This has a major impact on seismic-hazard analysis and seismotectonic interpretations in South Africa because both these fields depend on earthquake statistics, specifically the relative and absolute number of small to large earthquakes for a given source area or active fault system. A local magnitude scale is currently being developed for South Africa to address these shortcomings.

We further plan to determine one or more frequency-dependent attenuation relations to implement a M_w scale based on the Brune (1970) model for earthquakes in the range $\sim 2.5 < M_w < 4.0$ and derive an M_L–M_w relationship. Only three RMTs were determined for South Africa using data from the dense IRIS Kaapvaal craton array. Testing indicates that RMT with similar solutions to events 1 to 3 could be reliably obtained with only two stations within a 400-km radius and for an azimuth difference of at least 60°. The sparse, recently updated SANSN could in principle be used to calculate more RMTs. But, due to the low level of seismicity, no earthquake with adequate signal-to-noise ratio between 0.02 Hz and 0.1 Hz has been recorded to date.

The stable Kalahari craton might experience subtle heating and uplift owing to the African superplume and/or lithospheric modification at its base. The interior of southern Africa (except for Mozambique) has approximately 500 m positive residual elevation (Nyblade and Robinson 1994; Nyblade and Langston 1998). The African superplume is a large-scale,



▲ **Figure 14.** First-motion fault-plane solution for tectonic earthquake three in Table 1 that occurred in the Fauresmith area (left). Filled dots indicate compression and open dots dilatation. The oblique normal fault solution and stress directions are similar to the regional moment tensor in Figure 11. On the right the root-mean-square time residual is shown as a function of depth.

low-shear velocity anomaly that extends from the core-mantle boundary to about 1,500 km depth under eastern Africa, and viscous flow from the lower into the upper mantle is thought to uplift the surface here (*e.g.*, Simmons *et al*. 2007). The faulting regime in South Africa changes from normal faulting (extension) in the northeast near the east African rift to strike-slip faulting in the southwest (Figure 1). We interpret the moment tensors/focal mechanisms as follows: 1) In northeastern South Africa solutions are the result of crustal stresses associated with uplift/rifting even though the higher seismicity associated with the east African rift does not extend into the country. Stresses related to deep mining operations modify the normal faulting regime causing local volume closures. 2) Earthquake C with conflicting solutions C1 and C2 and different RMT no. 3 are situated at the change-over area to southwestern South Africa. 3) In southwestern South Africa, ridge push from the surrounding plate boundaries and/or local crustal thicknesses determines the stress regime.

CONCLUSIONS

We calculated three RMTs for South Africa and made progress toward resolving the discrepancy between local and moment magnitudes we observe for the SANSN. We conclude that moment tensors/focal mechanisms in South Africa change from normal faulting (extension) in the northeast near the east African rift to strike-slip faulting in the southwest.

ACKNOWLEDGMENTS

Moment tensors were computed using the mtpackagev1.1 package developed by Prof. Douglas Dreger of the Berkeley Seismological Laboratory, and Green's functions were computed using the FKRPROG software developed by Chandan Saikia of URS. Prof. Dreger provided us with a full moment-tensor inversion version of this software upon request. Figure 1 was created using Generic Mapping Tools (GMT) (Wessel and Smith 1991). We thank Lars Ottemöller from Bergen University, Norway, for the helpful discussions regarding regional moment-tensor analysis. We also wish to thank an anonymous reviewer for his many thoughtful suggestions.

REFERENCES

Aki, K., and P. G. Richards (1980). *Quantitative Seismology*. San Francisco: W. H. Freeman and Co., 932 pp.

Bernardi, F., J. Braunmiller, U. Kradolfer, and D. Giardini (2004). Automatic regional moment tensor inversion in the European-Mediterranean region. *Geophysical Journal International* **157**, 703–716.

Brune, J. N. (1970). Tectonic stress and spectra of seismic shear waves. *Journal of Geophysical Research* **75**, 4,997–5,009.

Braunmiller, J., and J. Nabelek (2002). Seismotectonics of the Explorer region. *Journal of Geophysical Research* **107** (B10), 2,208; doi:10.1029/2001JB000200.

Dreger, D. S. (2003). TDMT_INVC: Time domain seismic moment tensor INVersion. In *International Handbook of Earthquake and Engineering Seismology*, ed. W. H. K. Lee, **81B**, 1,627. Boston: Academic Press.

Dreger, D., and D. V. Helmberger (1993). Determination of source parameters at regional distances with single station or sparse network data. *Journal of Geophysical Research* **98**, 8,107–8,125.

Dziewonski, A. M., and D. L. Anderson (1981). Preliminary reference Earth model. *Physics of the Earth and Planetary Interiors* **25**, 297–356.

Dziewonski, A. M., G. Ekström, J. H. Woodhouse, and G. Zwart (1987). Centroid-moment tensor solutions for October–December 1986. *Physics of the Earth and Planetary Interiors* **48**, 5–17.

Dziewonski, A. M., G. Ekström, J. H. Woodhouse, and G. Zwart (1991). Centroid-moment tensor solutions for July–September 1990. *Physics of the Earth and Planetary Interiors* **67**, 211–220.

Fairhead, J. D., and R. W. Girdler (1971). The seismicity of Africa. *Geophysical Journal of the Royal Astronomical Society* **24**, 271–301.

Fairhead, J. D., and G. W. Stuart (1982). The seismicity of the east African rift system and comparison with other continental rifts. In *Continental and Oceanic Rifts*, ed. G. Pálmason, 41–61. Washington, DC: American Geophysical Union.

Fan, G., and T. Wallace (1995). Focal mechanism of a recent event in South Africa: A study using a sparse very broadband network. *Seismological Research Letters* **66**, 13–18.

Green, R. W. E., and A. McGarr (1972). A comparison of the focal mechanism and aftershock distribution of the Ceres, South Africa earthquake of September 29, 1969. *Bulletin of the Seismological Society of America* **62**, 869–871.

Hutton, L. K., and D. M. Boore (1987). The M_L scale in Southern California. *Bulletin of the Seismological Society of America* **77**, 2,074–2,094.

Johnson, M. R., C. R. Anhaeusser, and R. J. Thomas, eds. (2006). *The Geology of South Africa*. Johannesburg and Pretoria: Geological Society of South Africa and Council for Geoscience.

Jost, M. L., and R. Herrmann (1989). A student's guide to and review of moment tensors. *Seismological Research Letters* **60**, 37–57.

Julià, J., A. A. Nyblade, R. Durrheim, L. Linzer, R. Gök, P. Dirks, and W. Walter (2009). Source mechanisms of mine-related seismicity, Savuka mine, South Africa. *Bulletin of the Seismological Society of America* **99**, 2,801–2,814.

Kao, H., P.-R. Jian, K.-F. Ma, B.-S. Huang, and C.-C. Liu (1998). Moment tensor inversion for offshore earthquakes east of Taiwan and their implications to regional collision. *Geophysical Research Letters* **25**, 3,619–3,622.

Kennett, B. L. N., E. R. Engdahl, and R. Buland (1995). Constraints on seismic velocities in the Earth from travel times. *Geophysical Journal International* **122**, 108–124.

Kubo, A., E. Fukuyama, and K. Nonomuara (2002). NIED seismic moment tensor catalogue for regional earthquakes around Japan: Quality test and application. *Tectonophysics* **356**, 23–48.

Kwadiba, M. T. 0., C. Wright, E. M. Kgaswane, R. E. Simon, and T. K. Nguuri (2003). *Pn* arrivals and lateral variations of Moho geometry beneath the Kaapvaal craton. *Lithos* **71**, 393–411.

Larson, A. M., A. Snoke, and D. E. James (2006). *S*-wave velocity structure, mantle xenoliths, and the upper mantle beneath the Kaapvaal craton. *Geophysical Journal International* **167**, 171–186; doi:10.1111/j.1365-246X.2006.03005.x.

Li, A., and K. Burke (2006). Upper mantle structure of southern Africa from Rayleigh wave tomography. *Journal of Geophysical Research* **111**, B10303; doi:10.1029/2006JB004321.

Lienert, B. R. E., and J. Havskov (1995). A computer program for locating earthquakes both locally and globally. *Seismological Research Letters* **66**, 26–36.

Nguuri, T. K., J. Gore, D. E. James, S. J. Webb, C. Wright, T. G. Zengeni, O. Gwavava, J. A. Snoke, and Kaapvaal Seismic Group (2001). Crustal structure beneath southern Africa and its implication for the formation and evolution of the Kaapvaal and Zimbabwe cratons. *Geophysical Research Letters* **28**, 2,501–2,504.

Niu, F., and D. E. James (2002). Fine structure of the lowermost crust beneath Kaapvaal craton and its implications for crustal formation and evolution. *Earth and Planetary Science Letters* **200**, 12–30.

Nyblade, A., and C. A. Langston (1998). Upper mantle *P*-wave velocities beneath Southern Africa and the origin of the African superswell. *Southern African Geophysical Review* **2**, 55–61.

Nyblade, A., and S. Robinson (1994). The African superswell. *Geophysical Research Letters* **21**, 765–768.

Padhy, S. (2005), A scattering model for seismic attenuation and its global applications. *Physics of the Earth and Planetary Interiors* **148**, 1–12.

Pasyanos, M. E., D. S. Dreger, and B. Romanowicz (1996). Toward real-time determination of regional moment tensors. *Bulletin of the Seismological Society of America* **86**, 1,255–1,269.

Ratchkovski, N. A., and R. A. Hansen (2002). New constraints on tectonics of interior Alaska: Earthquake locations, source mechanisms, and stress regime. *Bulletin of the Seismological Society of America* **92**, 998–1,014.

Richter, C. F. (1935). An instrumental earthquake magnitude scale. *Bulletin of the Seismological Society of America* **25**, 1–32.

Ristau, J. (2008). Implementation of routine regional moment tensor analysis in New Zealand. *Seismological Research Letters* **79**, 400–415.

Ristau, J., G. C. Rogers, and J. F. Cassidy (2003). Moment magnitude local magnitude calibration for earthquakes off Canada's west coast. *Bulletin of the Seismological Society of America* **93**, 2,296–2,300.

Ristau, J., G. C. Rogers, and J. F. Cassidy (2007). Stress in western Canada from regional moment tensor analysis. *Canadian Journal of Earth Sciences* **44**, 127–148.

Romanowicz, B., D. Dreger, M. Pasyanos, and R. Urhammer (1993). Monitoring of strain release in central and northern California using broadband data. *Geophysical Research Letters* **20**, 1,643–1,646.

Saltzer, R. (2002). Upper mantle structure of the Kaapvaal craton from surface wave analysis—a second look. *Geophysical Research Letters* **29** (6); doi:10.1029/2001GL013702.

Saunders, I., M. B. C. Brandt, J. Steyn, D. L. Roblin, and A. Kijko (2008). The South African National Seismograph Network. *Seismological Research Letters* **79**, 203–210.

Shudofsky, G. N. (1985). Source mechanisms and focal depths of east African earthquakes using Rayleigh-wave inversion body-wave modeling. *Geophysical Journal of the Royal Astronomical Society* **83**, 563–614.

Simmons, N. A., A. M. Forte, and S. P. Grand (2007). Thermochemical structure and dynamics of the African superplume. *Geophysical Research Letters* **34**, L02301; doi:10.1029/2006GL028009.

Snoke, J. A. (2003) FOCMEC: FOCal MEChanism Determinations. In *International Handbook of Earthquake and Engineering Seismology,* ed. W. H. K. Lee, **81B**, 1,629–1,630. Boston: Academic Press.

Stankiewicz, J., S. Chevrot, R. D. Van der Hilst, and M. J. De Wit (2002). Crustal thickness, discontinuity, and upper mantle structure beneath southern Africa: Constraints from body wave inversions. *Physics of the Earth and Planetary Interiors* **130**, 235–251.

Wagner, G. S., and C. A. Langston (1988). East African earthquake body wave inversion with implications for continental structure and deformation. *Geophysical Journal* **94**, 503–518.

Wessel, P., and W. H. F. Smith (1991). Free software helps map and display data. *Eos, Transactions, American Geophysical Union* **72**, 441.

Wright, C., E. M. Kgaswane, M. T. O. Kwadiba, R. E. Simon, T. K. Nguuri, and R. McRae-Samuel (2003). South African seismicity, April 1997 to April 1999, and regional variations in the crust and uppermost mantle of the Kaapvaal craton. *Lithos* **71**, 369–392.

Wright, C., M. T. O. Kwadiba, E. M. Kgaswane, and R. E. Simon (2002). The structure of the crust and upper mantle to depths of 320 km beneath the Kaapvaal craton, from *P*-wave arrivals generated by regional earthquakes and mining-induced tremors. *Journal of African Earth Sciences* **35**, 477–488.

Council for Geoscience
Private Bag X112
Pretoria 0001
South Africa
martinb@geoscience.org.za
(M. B. C. B.)